RSC Advances

PAPER

View Article Online
View Journal | View Issue

Cite this: *RSC Adv.*, 2026, **16**, 23915

Nanoconfinement catalysis-enhanced electrochemiluminescence aptasensor for the sensitive detection of matrix metalloproteinase-9

Taoran Yan,[a] Xinying Ma[b] and Fengna Xi *[b]

Received 15th January 2026
Accepted 20th April 2026

DOI: 10.1039/d6ra00374e

rsc.li/rsc-advances

Matrix metalloproteinase-9 (MMP-9) detection is crucial for the early screening and treatment monitoring of infantile hemangioma. Herein, a nanoconfinement catalysis-enhanced electrochemiluminescence (ECL) aptasensor was fabricated for the sensitive detection of MMP-9. Co_3O_4 nanoparticles were electrochemically deposited onto an ordered silica nanochannel film (SNF), which not only exhibited electrocatalytic oxidation activity toward luminol and H_2O_2 but also possessed peroxidase (POD)-like activity. The synergistic effect between Co_3O_4 and the confinement effect of SNF remarkably amplified ECL from the luminol–H_2O_2 system. After functionalizing the electrode surface with epoxy groups, MMP-9 aptamers were covalently immobilized to construct the aptasensor. ECL signal quenching, attributable to the spatial hindrance and elevated interfacial resistance following the specific MMP-9/aptamer binding, served as the basis for the quantitative detection of MMP-9. The sensor displayed a wide linear response range (0.001 to 100 ng mL^{-1}), a low detection limit of 0.1 pg mL^{-1}, and high selectivity, reproducibility, and stability.

1. Introduction

Infantile hemangioma, a true vascular tumor, poses risks because of its unpredictable proliferative growth, which carries long-term psychosocial impact. Matrix metalloproteinases (MMPs) represent a family of zinc-dependent endopeptidases essential for degrading and remodeling the extracellular matrix (ECM), which participate in diverse physiological and pathological contexts.[1–3] Among MMPs, MMP-9 is a key enzyme that efficiently degrades type IV collagen, gelatin, and other major components of the basement membrane, making it an important mediator of tumor cell invasion and metastasis.[4–6] Its expression levels correlate strongly with infantile hemangioma. Creating sensitive and highly specific detection methods for MMP-9 holds significant value for the early screening, treatment monitoring and prognosis evaluation of infantile hemangioma.

MMP-9 can be detected by several established techniques,[7] including enzyme-linked immunosorbent assay (ELISA),[8] surface-enhanced Raman scattering (SERS),[9] and electrochemical methods.[10] While ELISA offers high specificity, it involves complex procedures. SERS is sensitive but often suffers from reproducibility issues due to substrate heterogeneity and may require complicated labelling processes. Electrochemical methods still face challenges related to signal reproducibility. Thus, a rapid, low-cost, highly sensitive, and user-friendly detection platform for MMP-9 detection is highly desirable.

Electrochemiluminescence (ECL) is a technique that triggers luminescent reactions when a potential is applied at the electrode surface, and it combines the precise control of electrochemical reactions with the high sensitivity of chemiluminescence.[11–14] ECL has several advantages, including low background signal, strong spatiotemporal control, and the ability to avoid light scattering and autofluorescence interference without the need for an external light source.[15–17] It has become a powerful tool for biomarker detection.[18–22] Among various ECL systems, the luminol–hydrogen peroxide (H_2O_2) system is widely used due to its low oxidation potential, low cost, and excellent biocompatibility.[23,24] However, the ECL efficiency of this system is often limited by reaction kinetics. Thus, enhancing the ECL signal, expanding the linear detection range, and reducing the detection limit have become critical areas of research.

Silica nanochannel films (SNFs) are highly ordered two-dimensional (2D) mesoporous materials, featuring a unique structure with uniform and regularly arranged nanochannels.[25–28] Owing to their mesochannels and high surface area, SNFs are ideal for the confinement and loading of nanomaterials.[29–32] By encapsulating nanoparticles in the channels of an SNF, a composite electrode interface can be constructed with the mass transport advantage of the nanochannel array. Thus, the electrocatalytic and enzyme-like dual

[a]*Department of Plastic and Burn Surgery, Shanxi Children's Hospital, Taiyuan, 030001, China. E-mail: tryan09@126.com*
[b]*School of Chemistry and Chemical Engineering, Zhejiang Sci-Tech University, Hangzhou 310018, China. E-mail: Fengnaxi@zstu.edu.cn*

catalytic activities of nanozymes can be combined to significantly enhance the ECL signal from the luminol–H_2O_2 system.

In this work, an MMP-9 aptasensor is fabricated based on SNF-confined Co_3O_4 nanozymes for enhanced ECL signal amplification. Co_3O_4 nanoparticles are confined within the channels of SNF modified on the ITO surface, which is electrochemically deposited, forming a Co_3O_4@SNF/ITO electrode. The amplification of the ECL signal and the catalytic mechanism of the system are systematically studied. By modifying the SNF surface with epoxy-silane, the MMP-9-specific aptamer is covalently immobilized, forming a highly selective sensor interface. Based on the ECL signal reduction caused by the MMP-9-induced spatial hindrance and interfacial resistance, this aptamer-based sensor enables the quantification of MMP-9, establishing a new strategy for its highly sensitive detection.

2. Experimental

2.1 Materials and reagents

Recombinant human MMP-9 protein and amino-modified MMP-9 aptamer (sequence: 5′-NH_2-TCGTATGGCACGGGGTTGGTGTTGGGTTGG-3′) were purchased from Shenggong Biotechnology Co., Ltd. Neutrophil gelatinase-associated lipocalin (NGAL) was obtained from Oke Biological. Tumor necrosis factor-alpha (TNF-α) and interleukin-1β (IL-1β) were purchased from Keyue Zhongkai. Potassium ferricyanide, cetyltrimethylammonium bromide (CTAB), potassium ferrocyanide, sodium hydroxide, tetraethyl orthosilicate (TEOS), (3-glycidyloxypropyl)trimethoxysilane (GPTMS), heptahydrate cobalt sulfate, luminol, bovine serum albumin (BSA), and H_2O_2 were obtained from Aladdin Biochemical Technology. All reagents were of analytical grade and used directly.

2.2 Characterizations and instrumentations

Morphological characterization was achieved through scanning electron microscopy (SEM, ZEISS Sigma 300) and transmission electron microscopy (TEM, Hitachi HT7700), while X-ray photoelectron spectroscopy (XPS, PHI 5300) was used for elemental analysis. An electrochemical workstation (Autolab PGSTAT302N) was used for cyclic voltammetry (CV) and electrochemical impedance spectroscopy (EIS) measurements. An electrochemiluminescence (ECL) analysis system (MPI-E II, Xian Ruimai) was used for ECL signal collection. A UV-vis spectrophotometer (Shimadzu UV-2450) was employed to verify the enzyme-like activity of the aptasensor.

2.3 Preparation of the SNF/ITO and Co_3O_4@SNF/ITO electrodes

Following a reported Stöber solution growth procedure,[33–35] SNF was deposited onto ITO by immersing the clean electrodes in a precursor mixture of CTAB, TEOS, and ethanol/water/ammonia at 60 °C for 24 h. After washing and drying at 100 °C for 12 h, the resulting surfactant-templated electrode (SM@SNF/ITO) was treated with a 0.1 M HCl–ethanol mixture under stirring to remove CTAB, leading to the formation of an SNF/ITO electrode featuring ordered open nanochannels. This electrode was then employed as the working electrode in 0.2 M $CoSO_4$, where a 3 s electrochemical deposition at +1.5 V produced the Co_3O_4@SNF/ITO composite electrode.

2.4 Fabrication of the aptasensor and ECL detection of MMP-9

First, epoxy groups were introduced onto the SNF surface by reacting the SM@SNF/ITO electrode with GPTMS in an ethanol solution (2.26 mM) in the dark for 1 h. After CTAB removal, Co_3O_4 was electrodeposited to yield the epoxy-modified Co_3O_4@O-SNF/ITO electrode. This electrode was subsequently incubated with the amino-modified MMP-9 aptamer at 4 °C for 90 min, washed with PBS, and then blocked with 0.5% BSA for 10 min at room temperature to minimize non-specific adsorptions, ultimately producing the final aptasensor BSA/Apt/Co_3O_4@O-SNF/ITO. For MMP-9 detection, this aptasensor was incubated with different concentrations of MMP-9. The ECL signal was measured using a phosphate buffer solution (PBS, 0.01 M, pH 7.4) containing luminol (100 μM) and H_2O_2 (100 μM).[30]

3. Results and discussion

3.1 Construction of the aptasensor and its detection strategy based on confinement catalysis-enhanced ECL

In this study, a high-performance ECL sensing interface was developed based on the synergistic effects of an ordered nanoconfinement catalysis and specific molecular recognition. As illustrated in Fig. 1, a highly ordered, vertically oriented silica nanochannel film was grown *in situ* on an ITO surface. This SNF featured uniform pore sizes and long-range ordered channels, providing a large specific surface area for subsequent biofunctionalization. The regular nanochannels also created one-dimensional spaces for facilitating material transport and confined reactions. As shown, prior to the removal of the surfactant template inside the channels, GPTMS with epoxy

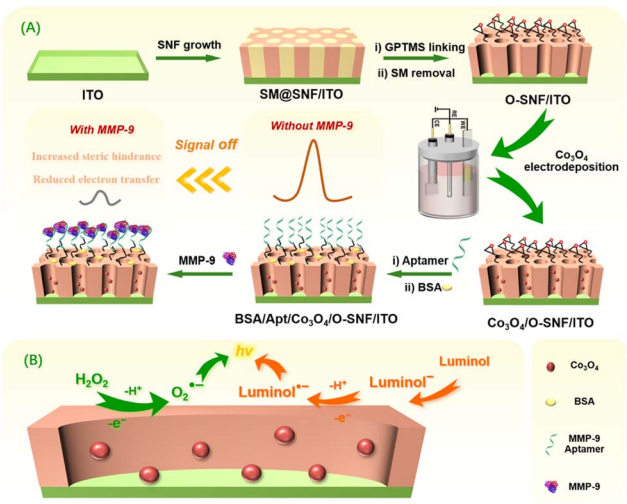

Fig. 1 Schematic of the aptasensor construction (A) based on enhanced ECL from the luminol–H_2O_2 system (B).

groups was used to functionalize the external surface of the SNF, specifically the pore entrance regions, to introduce highly reactive epoxy groups. This strategy ensured that the subsequent biomolecule immobilization reactions predominantly occurred at the nanochannel entrances, maintaining the internal channel accessibility, which was beneficial for the subsequent loading of nanozymes and mass transport.

The strategy of enhancing ECL through confinement catalysis is critical for improving the sensor performance. Co_3O_4 was introduced into the SNF by one-step potentiostatic electrodeposition. On the one hand, the pore walls of the SNF physically restricted the growth and migration of the Co_3O_4 nanoparticles, anchoring them in a highly dispersed state within the channels. This effectively prevented nanoparticle aggregation and exposed more electrochemical active sites. On the other hand, the confined Co_3O_4 nanoparticles possessed significantly enhanced catalytic properties within the nano-confinement space, resulting in ECL signal amplification.

The ECL detection strategy is based on the combination of enhanced ECL signal generation and high specificity recognition. The epoxy groups pre-modified on the surface of the SNF covalently interacted with the amino groups at the 3′ end of the MMP-9 aptamer, thereby immobilizing the aptamer selectively at the entrance region of the nanochannels. When the target analyte MMP-9 was present, it bonded to the aptamer with high affinity and specificity, forming a biomolecular complex layer. This complex layer caused significant steric hindrance, physically blocking the diffusion of luminol/H_2O_2 within the channels and increasing the interfacial resistance. This decrease in mass transport and rise in electron transfer resistance, triggered by the biomolecular recognition, lead to a reduction in the ECL signal. Using this principle, MMP-9 could be quantitatively detected.

3.2 Morphological, structural, and compositional characterization of electrode materials

The morphology of SNF/ITO is shown in Fig. 2. The top-view TEM image (Fig. 2A) clearly reveals that the fabricated SNF/ITO electrode has a highly ordered, uniformly distributed array of nanochannels, with hexagonal close packing of the channels. A further observation of the TEM cross-sectional image (Fig. 2B) shows that these nanochannels are oriented vertically to the substrate, with a uniform film thickness of approximately 98 nm. The cross-sectional SEM image (Fig. 2C) clearly displays the SNF layer/ITO layer/glass layer sandwich structure, with the SNF layer having a thickness of approximately 99 nm, which closely matches the TEM result.

SEM images of the electrode before and after Co_3O_4 deposition (Fig. 2D and E) show that the Co_3O_4@SNF/ITO surface remains smooth and clean, with no significant nanoparticle aggregation or pore blockage. This suggests that the Co_3O_4 deposition occurred predominantly within the SNF nanochannels and not on the external surface. Fig. 2F presents the TEM image of Co_3O_4@SNF. Compared with that of SNF, no apparent surface change was observed on Co_3O_4@SNF, which further indicated that Co_3O_4 was confined within the nanochannels. Elemental mapping revealed a homogeneous distribution of Si, O, and Co (Fig. 2G), confirming the uniform dispersion of Co_3O_4 within the nanochannels of the SNF.

X-ray photoelectron spectroscopy (XPS) analysis was also conducted. The spectrum of Co_3O_4@SNF/ITO exhibited new characteristic peaks corresponding to the Co 2p and Co 3p orbitals with an atomic Co content of 2.1% (Fig. 3A), which suggests the presence of the cobalt element. The high-resolution Co 2p spectrum (Fig. 3B) revealed a pair of spin–orbit split peaks at 780.7 eV and 795.9 eV, attributed to Co^{3+} and another pair of peaks at 782.1 eV and 797.8 eV associated with Co^{2+}.[36] Additionally, prominent satellite peaks near 786 eV and 803 eV are typical features of Co^{2+} species in Co_3O_4.[37]

Further electrochemical analysis confirmed the electrochemical activity of Co_3O_4. In an NaOH solution, the cyclic voltammetry (CV) curve obtained for the SNF/ITO electrode displayed no obvious redox peaks (Fig. 3C). In contrast, the Co_3O_4@SNF/ITO electrode exhibited two pairs of distinct reversible redox peaks. Peak I (~0.1 V *vs.* Ag/AgCl) corresponded to the conversion between Co^{3+} and Co^{2+} ($Co_3O_4 + H_2O + e^- \rightleftharpoons 3CoOOH + OH^-$), while peak II (~0.5 V *vs.* Ag/AgCl) was associated with Co^{4+}/Co^{3+} conversion ($CoOOH - e^- \rightleftharpoons CoO_2 + H^+$).[38] The appearance of these two characteristic peaks confirmed that the redox-active Co_3O_4 has been successfully deposited.

3.3 Mechanism of ECL enhancement by Co_3O_4@SNF/ITO

The control electrode using Co_3O_4 without SNF confinement was fabricated, and its ECL signal was investigated. As shown in Fig. S1A (SI), the peak current of Co_3O_4 at 0.5 V on the

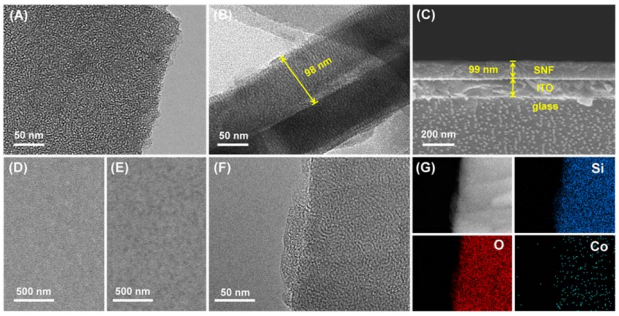

Fig. 2 TEM images showing the top view (A) and cross-section (B) of SNF/ITO. (C) SEM image of the SNF/ITO cross-section. (D) Top-view SEM images of SNF/ITO and (E) Co_3O_4@SNF/ITO. (F) Top-view TEM image of Co_3O_4@SNF. (G) EDS elemental mapping of Co_3O_4@SNF.

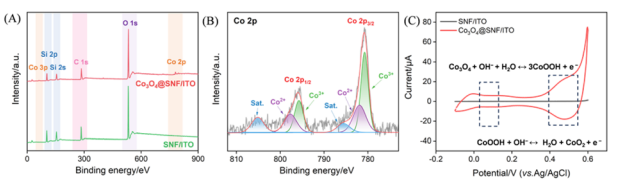

Fig. 3 (A) XPS spectra of SNF/ITO and Co_3O_4@SNF/ITO. (B) High-resolution Co 2p energy spectrum of SNF/ITO and Co_3O_4@SNF/ITO. (C) CV curves of SNF/ITO and Co_3O_4@SNF/ITO in 1 M NaOH.

Co_3O_4@ITO electrode is nearly identical to that on the Co_3O_4@SNF/ITO electrode (Fig. 3C), indicating comparable Co_3O_4 loadings on both the electrodes. As presented in Fig. S1B, the ECL signal measured at the Co_3O_4@ITO electrode was twice that of the ITO electrode, while the Co_3O_4@SNF/ITO electrode exhibited an ECL signal six times higher than that of the SNF/ITO electrode. Moreover, the ECL intensity of Co_3O_4@SNF/ITO was significantly higher than that of Co_3O_4@ITO. These results demonstrated that Co_3O_4 confined within the SNF nanochannels exhibited enhanced catalytic activity. Additionally, during consecutive ECL measurements, the signal at the Co_3O_4@ITO electrode gradually decreased, with a relative standard deviation (RSD) of 11% over seven cycles, indicating poor stability and detachment of Co_3O_4 deposited on ITO (Fig. S1C). In contrast, the Co_3O_4@SNF/ITO electrode maintained high stability under continuous measurements with an RSD of 1.9% (Fig. S1C), confirming the good stability of Co_3O_4 confined within the nanochannels. These results suggested that nanoconfinement within the SNF channels enhanced both the catalytic activity and stability of Co_3O_4.

An electrochemical method was used to investigate the mechanism behind the Co_3O_4-amplified ECL signal. As shown in Fig. 4B and C, SNF/ITO exhibited almost no current response in H_2O_2 solution, while the Co_3O_4@SNF/ITO electrode produced a current of 5.9 μA. After subtracting the current of 2.3 μA from the Co_3O_4@SNF/ITO electrode, which was due to the oxygen evolution reaction in PBS, the increase of 3.6 μA in current demonstrated that Co_3O_4 has an electrocatalytic oxidation activity toward H_2O_2. In contrast, Co_3O_4@SNF/ITO has a current signal of 21.2 μA in the luminol solution. A net current increase of 17.3 μA, after subtracting the background currents from luminol on SNF/ITO (1.6 μA) and Co_3O_4@SNF/ITO in PBS (2.3 μA), confirmed the electrocatalytic activity of Co_3O_4 toward luminol oxidation.

To investigate the influence of the electroactive area on the enhancement of the ECL signal, the electroactive area was determined by recording the peak current of the electrode in an FcMeOH probe solution. As shown in Fig. 5A and B, the electroactive areas of both electrodes were calculated using the Randles–Sevcik equation:[39,40]

$$I_p = 2.69 \times 10^5 \times A \times D^{1/2} \times n^{3/2} \times \nu^{1/2} \times C$$

Here, A denotes the electroactive area; D is the diffusion coefficient of FcMeOH; n represents the number of electrons transferred ($n = 1$); ν stands for the scan rate; and C corresponds to the molar concentration of FcMeOH. The calculated ratio of the electroactive area before and after Co_3O_4 deposition was 0.93, showing little change. This suggested that the increase in ECL signal in the luminol–H_2O_2 system is not primarily due to changes in the electroactive area but rather due to the electrocatalytic effects of Co_3O_4 on luminol and H_2O_2.

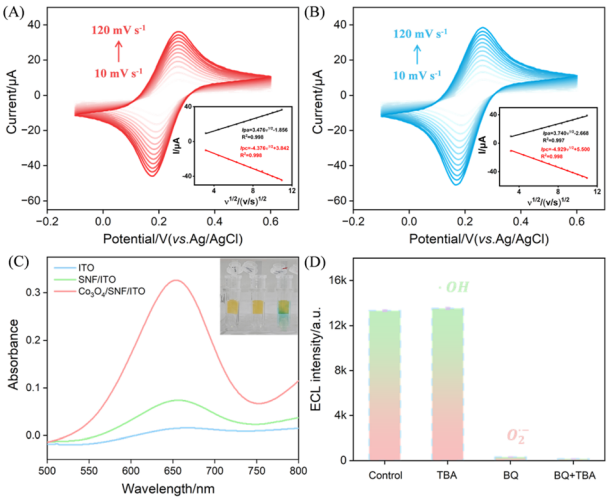

Fig. 5 CV responses of (A) SNF/ITO and (B) Co_3O_4@SNF/ITO in 0.5 mM FcMeOH at varied scan rates (insets: peak current *vs.* square root of the scan rate). (C) UV-vis absorption spectra of different systems in an NaAc/HAc buffer at pH 4.0 containing 1 mM H_2O_2 and 0.25 mM TMB (inset: color change after a 5 min reaction with the electrode). (D) ECL signals of Co_3O_4@SNF/ITO with different ROS scavengers: 100 μM BQ and 100 μg per mL TBA.

The peroxidase-like activity of the Co_3O_4@SNF/ITO electrode was confirmed by its catalytic activity for the oxidation of TMB to oxTMB in the presence of H_2O_2 (Fig. 5C). This activity, which promotes ROS generation from H_2O_2, is expected to contribute to the ECL signal enhancements. The involvement of the specific ROS was further examined using scavengers including *tert*-butyl alcohol (TBA) for hydroxyl radicals ($^{\bullet}OH$) and benzoquinone (BQ) for superoxide anion radicals ($O_2^{\bullet-}$). As shown in Fig. 5D, the addition of BQ significantly reduced the ECL signal, confirming that the superoxide anion radical plays a key role in the signal enhancement.[41,42] The ECL signal of the Co_3O_4@SNF/ITO electrode was measured in the absence of an applied potential (Fig. S2). As shown, no ECL signal was generated under potential-free conditions. This was because the nanozyme solely catalyzed the generation of ROS from H_2O_2 but did not catalyze the oxidation of luminol. Thus, the application of a potential to oxidize luminol, in combination with the nanozyme-based ROS generation, is required to produce an ECL signal.

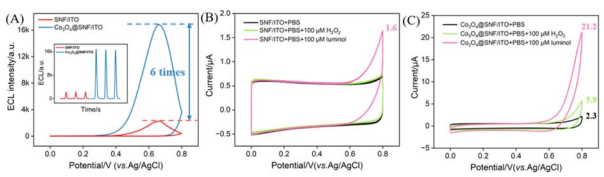

Fig. 4 (A) Comparison of the ECL signal intensities for different electrodes (inset: corresponding ECL time curves). (B) CV curves of SNF/ITO and (C) Co_3O_4@SNF/ITO in PBS (0.01 M, pH 7.4), PBS + 100 μM H_2O_2, and PBS + 100 μM luminol at 100 mV s^{-1}.

3.4 Construction of the aptasensor and the feasibility of MMP-9 detection

CV, EIS, and DPV measurements in an $Fe(CN)_6^{3-/4-}$ solution were used to monitor each fabrication step and MMP-9 incubation (Fig. 6A–D). In CV and DPV measurements (Fig. 6A and

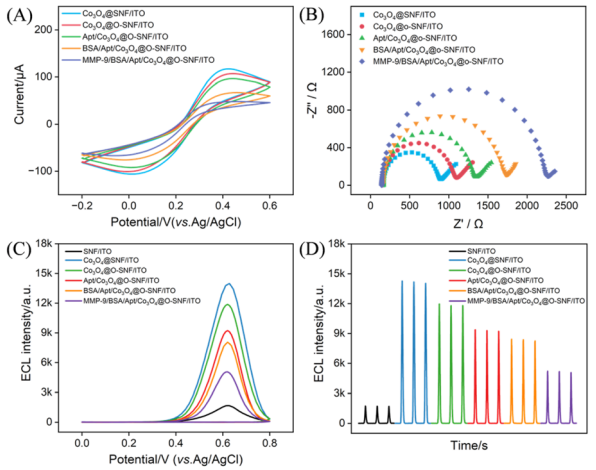

Fig. 6 (A) CV and (B) EIS profiles of different electrodes in 0.1 M KCl with 2.5 mM $Fe(CN)_6^{3-/4-}$. (C) ECL–potential and (D) ECL–time curves for different electrodes in PBS containing 100 μM luminol and 100 μM H_2O_2 (MMP-9 concentration: 1 ng mL^{-1}).

C), the current signal exhibited a progressive reduction following the successive modifications with epoxy groups, aptamer immobilization, BSA blocking, and MMP-9 binding. This decrease in current signal was attributed to the increasing spatial hindrance and interface resistance on the electrode surface, which made diffusion and electron transfer more difficult,[43–45] thereby confirming the successful modification at each step. The gradually increasing charge transfer resistance (R_{ct}) values in Fig. 6B and the decreased ECL signals in Fig. 6D further validate the successful modification of the sensor and MMP-9 binding at each step.

3.5 Optimization of detection conditions for MMP-9

To achieve optimal detection performance, the deposition time of Co_3O_4, the incubation time and concentration of the aptamer in aptamer immobilization, and the incubation time between MMP-9 and the aptamer sensor were optimized (Fig. S3 in the SI). The ECL signal initially increased and then decreased with increasing Co_3O_4 deposition time owing to the small amount of the nanocatalyst at low deposition times and the presence of large particles or blocking of nanochannels at high deposition times (Fig. S1A). A deposition time of 3 seconds was selected as the optimal condition for Co_3O_4 deposition. Fig. S1B and C show the optimization of aptamer incubation time and concentration, respectively. Both parameters exhibited an initial decrease followed by stabilization, indicating that the aptamer modification reached its maximum. Thus, the optimal incubation time for the aptamer was chosen as 90 min, and the optimal concentration was 0.4 μM. Fig. S3D illustrates the optimization of MMP-9 incubation time, where the incubation reached its maximum at 90 min. Thus, 90 min was selected. The ECL response of the Co_3O_4@SNF/ITO electrode as a function of pH was investigated and presented in Fig. S4 (SI). As observed, negligible ECL signals were detected under acidic conditions. This could be attributed to the fact that luminol cannot be deprotonated in an acidic environment, thereby failing to initiate the ECL reaction. In contrast, the ECL signal increased significantly under alkaline conditions. However, in this study, due to the high catalytic activity of the confined Co_3O_4 nanozymes, luminol generates a robust ECL signal even under neutral conditions. This study involves an aptamer-antigen recognition-based bioassay, where antigen activities and interactions are more effectively preserved in near-neutral environments. Additionally, the pH of serum, a biological sample, is approximately 7.4. Moreover, the stability of the silica structure in VMSF decreases under strong alkaline conditions. Thus, near-neutral conditions (pH 7.4), which are commonly used in bioanalytical applications, were selected for the analysis.

3.6 ECL detection of MMP-9 and real sample analysis

Under optimal conditions, the response of the constructed aptasensor to MMP-9 was assessed. As shown in Fig. 7A, higher MMP-9 concentrations resulted in greater antigen binding on the electrode surface. This consequently improved steric hindrance and interfacial resistance, which impeded both mass transport and electron transfer, thus gradually reducing the ECL signal. Fig. 7B presents the calibration curve, revealing a good linear correlation between ECL signal intensity (I_{ECL}) and the logarithm of the MMP-9 concentration ($\log C_{MMP\text{-}9}$) in the range of 100 ng mL^{-1} to 1 pg mL^{-1}. The limit of detection (LOD) was found to be 0.1 pg mL^{-1}. The limit of detection (LOD) was calculated based on the IUPAC definition ($X_L = X_B + kS_B$), where X_L is the minimum detectable signal, and X_B and S_B are the mean and standard deviation of the blank measurements. Using this value in the calibration plot, the LOD was determined to be 0.1 pg mL^{-1} at a signal-to-noise ratio of 3 (S/N = 3).

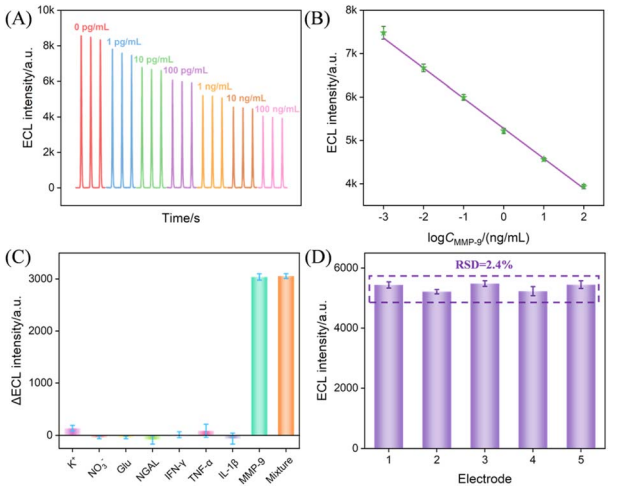

Fig. 7 (A) ECL responses of the aptasensor to different MMP-9 concentrations. (B) Corresponding calibration curve. Error bars represent standard deviation from three detections (n = 3). (C) ECL intensity change before and after incubation with potential interferents, such as K^+ (100 nM), NO_3^- (100 nM), Glu (100 nM), NGAL (10 ng mL^{-1}), IFN-γ (10 ng mL^{-1}), TNF-α (10 ng mL^{-1}), IL-1β (10 ng mL^{-1}), MMP-9 (1 ng mL^{-1}), or their mixtures. (D) Reproducibility of the aptasensor in detecting 1 ng per mL MMP-9.

Compared with other previously reported sensors, the proposed MMP-9 aptasensor exhibited a wider detection range and a lower LOD (Table S1 in SI). Additionally, this aptasensor offers additional advantages including facile fabrication, low construction cost, and no need for expensive antibodies.

The selectivity and anti-interference performance of the sensor were assessed against common serum interferents, including ions, electroactive species, and biomarkers. As shown in Fig. 7C, no significant ECL signal decrease was observed when MMP-9 was absent from the tested solution. A decrease in the ECL signal occurred only when MMP-9 or a mixture of MMP-9 with interferents was present, demonstrating that the sensor exhibits excellent selectivity and resistance to interference. Additionally, five parallelly fabricated electrodes yielded consistent signals (RSD = 2.4%) for 1 ng per mL MMP-9 (Fig. 7D), demonstrating excellent intra-batch reproducibility. The inter-batch reproducibility of the sensor was evaluated by testing five electrodes prepared from different batches. The RSD for MMP-9 (1 ng mL^{-1}) detection using these electrodes was obtained to be 3.5%, demonstrating good inter-batch reproducibility of the proposed sensor. The storage stability of the sensor was evaluated by storing seven identically prepared aptasensors at 4 °C. One electrode was taken out each day to detect 1 ng mL^{-1} of MMP-9. The ECL signal retained 90% of its initial value after 7 days of storage, demonstrating good storage stability of the proposed sensor.

The feasibility of applying the ECL sensor to real-sample analysis was investigated using fetal bovine serum (FBS) and the standard addition method. The analysis yielded recoveries between 102% and 108%, with RSDs under 3.0% for triplicate measurements (see Table S2, SI), validating the method's reliability in complex biological environments.

4. Conclusions

In this work, a highly sensitive aptasensor based on Co_3O_4-confined catalytic enhancement of ECL was successfully developed for the detection of MMP-9. The ordered silica nanochannels not only served as a confined support for Co_3O_4, preventing its aggregation, but also provided a structured mass transfer pathway. The synergistic effect between the electrocatalytic and enzyme-like catalytic properties of Co_3O_4 significantly enhanced the ECL signal in the luminol–H_2O_2 system. The constructed aptasensor exhibited high sensitivity, good selectivity, and ease of operation, offering a new approach for the clinical detection of cancer biomarkers.

Conflicts of interest

There are no conflicts to declare.

Data availability

The authors confirm that the data supporting the findings of this study are available within the article.

Supplementary information (SI) is available. See DOI: https://doi.org/10.1039/d6ra00374e.

Acknowledgements

The authors gratefully acknowledge the National Natural Science Foundation of China (22374130).

References

1 H. Laronha and J. Caldeira, *Cells*, 2020, **9**, 1076.
2 M. S. Ågren and U. auf dem Keller, *Int. J. Mol. Sci.*, 2020, **21**, 2678.
3 L. G. N. de Almeida, H. Thode, Y. Eslambolchi, S. Chopra, D. Young, S. Gill, L. Devel and A. Dufour, *Pharmacol. Rev.*, 2022, **74**, 714–770.
4 S. Mondal, N. Adhikari, S. Banerjee, S. A. Amin and T. Jha, *Eur. J. Med. Chem.*, 2020, **194**, 112260.
5 Z. A. Rashid and S. K. Bardaweel, *Int. J. Mol. Sci.*, 2023, **24**, 12133.
6 M. M. Mubarak, I. A. Baba, Z. A. Wani, H. A. Kantroo and Z. Ahmad, *Int. J. Biol. Macromol.*, 2025, **311**, 143902.
7 H. Zhang, M. Wu, H. T. Ta, Z. P. Xu and R. Zhang, *Adv. Mater. Technol.*, 2023, **8**, 2201786.
8 Y. Ding, Q. Tian, Y. Dong, L. Xing, S. C. B. Gopinath and Y. Mao, *Process Biochem.*, 2021, **100**, 231–236.
9 H. Jin, T. Liu and D. Sun, *Microchim. Acta*, 2024, **191**, 105.
10 L. Xiang, W. Cheng, J. Zhang, X. Li, A. Khan, Y. Yi and J. Li, *Biosens. Bioelectron.*, 2023, **237**, 115455.
11 Z. Zhang, P. Du, G. Pu, L. Wei, Y. Wu, J. Guo and X. Lu, *Mater. Chem. Front.*, 2019, **3**, 2246–2257.
12 J. Huang, T. Zhang, Y. Zheng and J. Liu, *Biosensors*, 2023, **13**, 317.
13 J. Huang, S. Xu, F. Yan and J. Liu, *Sens. Actuators, B*, 2024, **402**, 135119.
14 X. Luo, T. Zhang, H. Tang and J. Liu, *Front. Nutr.*, 2022, **9**, 962736.
15 W. Miao, *Chem. Rev.*, 2008, **108**, 2506–2553.
16 J. Li, H. Lin, F. Yan and L. Cui, *Microchim. Acta*, 2026, **193**, 285.
17 C. Wei, Y. Zheng, F. Yan and L. Xu, *Biosensors*, 2025, **15**, 332.
18 R. Yu, Y. Zhao and J. Liu, *Nanomaterials*, 2024, **14**, 390.
19 J. Gong, T. Zhang, T. Luo, X. Luo, F. Yan, W. Tang and J. Liu, *Biosens. Bioelectron.*, 2022, **215**, 114563.
20 J. Gong, T. Zhang, P. Chen, F. Yan and J. Liu, *Sens. Actuators, B*, 2022, **368**, 132086.
21 X. Zhou, X. Gu, S. Zhang, Y. Zou and F. Yan, *Microchem. J.*, 2024, **200**, 110315.
22 Z. Shi, T. Zhang, Y. Zhao, Y. Zhou and J. Liu, *Biosens. Bioelectron.*, 2025, **288**, 117828.
23 X. Fan, J. Wu, T. Zhang and J. Liu, *ChemBioChem*, 2024, **25**, e202400320.
24 Y. Cui, L. Huang, J. Zhao, J. Liu and W. Hu, *Rare Met.*, 2026, **45**, e70269.
25 L. Wang, S. Gu, F. Yan and C. Shen, *Microchem. J.*, 2026, **220**, 116658.
26 J. Huang, X. Fan, F. Yan and J. Liu, *ACS Appl. Nano Mater.*, 2024, **7**, 7743–7752.
27 J. Huang, T. Zhang, G. Dong, S. Zhu, F. Yan and J. Liu, *Front. Chem.*, 2022, **10**, 900282.

28 X. Deng, X. Lin, H. Zhou, J. Liu and H. Tang, *Nanomaterials*, 2023, **13**, 239.
29 X. Zhou, Y. Zou, H. Ru, F. Yan and J. Liu, *Anal. Chem.*, 2024, **96**, 10264–10273.
30 Y. Zhou, C. Zhang, J. Liu and Y. Mou, *Talanta*, 2025, **285**, 127223.
31 C. Zhang, X. Zhou, F. Yan and J. Lin, *Molecules*, 2023, **28**, 6443.
32 H. Wang, H. Wang and F. Yan, *RSC Adv.*, 2026, **16**, 501.
33 Z. Teng, G. Zhe ng, Y. Dou, W. Li, C. Y. Mou, X. Zhang, A. M. Asiri and D. Zhao, *Angew. Chem., Int. Ed.*, 2012, **124**, 2215–2219.
34 J. Wu, C. Li, J. Zhao and J. Liu, *Microchim. Acta*, 2026, **193**, 134.
35 J. Wu, T. Zhang, X. Jia, J. Li, H. Xie, F. Yan, D. Li and J. Liu, *J. Colloid Interface Sci.*, 2026, **701**, 138721.
36 l. Huang, X. Gu and F. Xi, *J. Electroanal. Chem.*, 2026, **1006**, 119896.
37 R. Shu, L. Nie, X. Liu and K. Chen, *J. Mater. Sci. Technol.*, 2024, **190**, 106–116.
38 A. Salimi, H. Mamkhezri, R. Hallaj and S. Soltanian, *Sens. Actuators, B*, 2008, **129**, 246–254.
39 X. Fan, T. Zhang, S. Wang, Y. Jiang, Y. Zhao, F. Yan and F. Xi, *Sens. Actuators, B*, 2025, **439**, 137856.
40 X. Fan, L. Wang, H. Wang, L. Huang, J. Lin, X. Gao and F. Xi, *Biosens. Bioelectron.*, 2025, **280**, 117451.
41 J. Zhao, X. Gu and J. Liu, *Microchem. J.*, 2025, **216**, 114671.
42 C. Lu, X. Jia, F. Yan and Y. Zhou, *Electrochim. Acta*, 2026, **551**, 148136.
43 T. Zhang, J. Gong, Q. Han, W. Hu, F. Yan and J. Liu, *Talanta*, 2024, **277**, 126319.
44 J. An, C. Zhang, F. Yan and P. Ma, *Microchem. J.*, 2024, **206**, 111413.
45 C. Zhu, H. Wang and J. Liu, *Front. Chem.*, 2025, **13**, 1549927.